Energy Materials and Devices

Open Access
Research Article

Graphical Abstract

Step-by-step procedure and criteria for a *p–n* junction solar cell design

Carlos Villa-Angulo ✉

Institute of Engineering, Universidad Autónoma de Baja California (UABC), Mexicali, BC 21280, Mexico

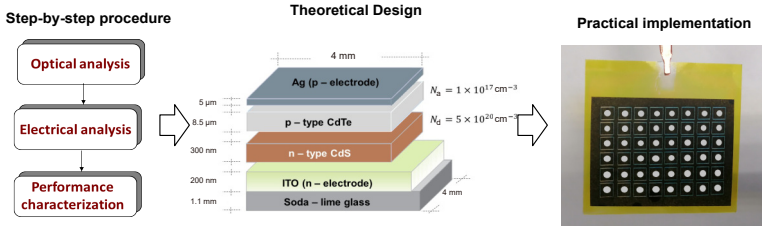

A step-by-step procedure for a solar cell design, fabrication and characterization is presented. The presented procedure is complemented with designing criteria and numerical modeling and simulation algorithms. A CdS/CdTe heterojunction material is used for practical implementation, and the exciton generation rate $G(x, \lambda)$ to define correlation and optimization rules.

✉Address correspondence to **Carlos Villa-Angulo**, villac@uabc.edu.mx

Received: November 16, 2025
Revised: December 28, 2025
Accepted: January 7, 2026

9370087

Read Online

Citation: villa-Angulo C. Step-by-step procedure and criteria for a *p–n* junction solar cell design. *Energy Mater. Devices*, 2026, 4(1), 9370087. https://doi.org/10.26599/EMD.2026.9370087

Energy Materials and Devices
https://doi.org/10.26599/EMD.2026.9370087
Open Access
Research Article

Step-by-step procedure and criteria for a *p–n* junction solar cell design

Carlos Villa-Angulo ✉

Institute of Engineering, Universidad Autónoma de Baja California (UABC), Mexicali, BC 21280, Mexico

Cite this article: *Energy Mater. Devices* 2026, **4**(1): 9370087. https://doi.org/10.26599/EMD.2026.9370087

ABSTRACT

Abstract. A theoretical *p–n* junction photovoltaic device design procedure is proposed. The procedure comprises optical and electrical analyses to determine the device structure, including material selection, layer dimensions, doping concentrations, and performance characterization. This procedure is complemented by designing criteria, numerical modeling, and simulation algorithms. The practical implementation, including physical fabrication and practical measurements, was performed. A cadmium sulfide/cadmium telluride heterojunction film is used for the practical implementation, and the exciton generation rate is used to determine the improvement and optimization rules. Further, a correlation of theoretical and practical results is realized based on the improvement and optimization rules. The obtained results demonstrate the functionality of the proposed procedure, which can be adapted for different device structures and materials. The findings of this study are of great interest to designers and engineers interested in correlating theoretical results with practical measurements.

KEYWORDS

p-n junction, solar cell design, step-by-step designing procedure, CdS/CdTe heterojunction

1 Introduction

As an efficient alternative to fossil fuels, photovoltaic (PV) devices, also known as solar cells, are one of today's most promising clean energy sources[1–4]. Because solar energy is renewable and inexhaustible, PV devices do not emit polluting gases during operation, unlike fossil fuels that release large amounts of carbon dioxide (CO_2) and other pollutants when burned, contributing to climate change[5–7]. Moreover, the cost of solar energy has reduced in the past decade; in several regions, it is now cheaper to generate electricity with solar panels than with coal or gas plants[8,9]. A PV device converts sunlight into electricity based on the photoelectric effect. The active part of a PV device comprises a *p–n* junction illuminated to absorb photons from incident light and release electrons that generate an electric current. The *p–n* junction can be a homojunction (the same material *p* and *n* components) or a heterojunction (different material *p* and *n* components). Figure 1 shows the standard structures of a single PV device and a multi-PV device panel. Each structure comprises the following:

(1) A *p*-type electrode top layer, which comprises a conductive metal that functions as a low contact. The *p*-type electrode must have a large work function to form a good ohmic contact with a *p*-type semiconductor[10]. Common materials used for this purpose are gold (Au), silver (Ag), copper (Cu), and aluminum (Al).

(2) A *p*-type material layer, which is responsible for generating excitons (electron–hole pair generation via photon absorption). This layer is also called the active layer due to its function of absorbing the greatest amount of solar radiation to generate photocurrent[11]. Examples of materials used for this layer are *p*-type-doped silicon (Si-*p*), *p*-type-doped gallium arsenide (GaAs-*p*), *p*-type-doped cadmium selenide (CdSe-*p*), and *p*-type-doped cadmium telluride (CdTe-*p*).

(3) An *n*-type material layer, which is also called the window layer because it comprises a highly photoconductive material that allows the greatest amount of solar radiation to pass to the active layer[12,13]. This layer, together with the active layer, forms the *p–n* junction. Common materials used for this layer are *n*-type-doped silicon (Si-*n*), *n*-type-doped gallium arsenide (GaAs-*n*), and *n*-type-doped cadmium sulfide (CdS-*n*).

(4) An *n*-type electrode, which is a transparent conductive oxide (TCO) that functions as a first contact material. This layer is transparent to avoid attenuation in light incident on PV devices. Examples of materials used for this layer are zinc oxide (ZnO), indium-doped tin oxide (ITO), and fluorine-doped tin oxide (FTO)[14,15].

(5) A substrate layer, which must be a highly transparent material with sufficient thermal rigidity characteristics to support the other layers. This layer is commonly made of soda-lime glass.

Received: November 16, 2025 / **Revised:** December 28, 2025 / **Accepted:** January 7, 2026

✉**Address correspondence to** Carlos Villa-Angulo, villac@uabc.edu.mx

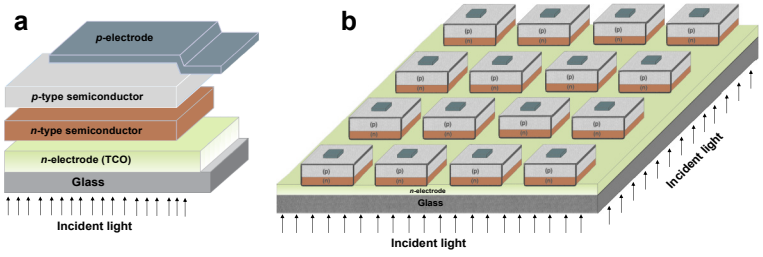

Figure 1 PV structures. (a) Single PV device. (b) Multi-PV device panel.

The design objective of a PV device is to determine the device structure, including the materials, layer dimensions, doping concentrations, and performance characterization parameters from a set of input parameters. The input parameters include the incident radiation spectrum, incident optical power, voltage, current, and electrical power to be delivered by the PV device. The layer dimensions comprise the physical dimensions of each layer, including thickness, width, and length. Various numerical simulators, such as Silvaco ATLAS, COMSOL, ADEPT, AMPS-1D, AFORS-HET, ASPIN, PC1D, PECSIM, SCAPS-1D, SETFOS, and DESSIS, are available for modeling a PV device[16–19]. Almost all these simulators solve the standard PV device equations and models with appropriate boundary conditions. Depending on the PV device's internal or external phenomenon to be simulated, each simulator has some advantages and disadvantages over the others. In addition, online educational platforms that offer PV device working principles with constraints, theoretical models, and simulation methods, such as PVLighthouse and PVEducation, are available[16]. Nevertheless, it is uncommon to find a design guideline that includes the criteria for selecting materials, layer dimensions, and doping concentrations as well as theoretical–practical result correlation. Similar to numerical simulations, theoretical design procedures allow researchers to predict and optimize PV device performance without physical testing. Theoretical design is essential for analyzing and optimizing PV device performance, avoiding the high cost and time associated with physical manufacturing[20,21]. In this study, a theoretical step-by-step PV device design procedure is proposed. The procedure is complemented with simulation algorithms. A CdS/CdTe heterojunction PV device is designed to demonstrate the procedure's functionality. We consider the exciton generation rate $G(x, \lambda)$ as a function of position (x) and wavelength (λ) to determine improvement and optimization rules.

2 Theoretical design of a *p–n* junction PV device

Figure 2 shows a block diagram of the proposed step-by-step procedure. The procedure comprises three main processes. The first is an optical analysis to determine $G(x, \lambda)$ in the photon absorber region. An optical transfer matrix is used in this process to analyze the optical electromagnetic field propagation and dissipation in the multilayer structure that forms the PV device. The second is an electrical analysis to determine the charge concentrations, electrostatic potential, and depletion zone dimensions of the *p–n* junction under optical stimulation (out of thermal equilibrium). The third is determining the performance characterization parameters, including open-circuit voltage (V_{oc}), short-circuit current density (J_{sc}), fill-factor (FF), and power conversion efficiency (PCE). The details of each process are described in the following sections.

2.1 Optical analysis (modeling and extraction of $G(x, \lambda)$)

The input parameters required by the proposed procedure are the incident light spectrum, average optical power, load resistance, and voltage to be delivered by the PV device at maximum power. The light spectrum and average optical power are obtained from an AM0 standard spectrum for space applications with an integrated average optical power of 1366.1 W/m^2, AM1.5 Global (AM1.5G) spectrum designed for flat plate modules with an integrated power of 1000 W/m^2, or AM1.5 Direct spectrum defined for solar concentrator work with an average integrated power density of 900 W/m^2. Therefore, the current at maximum power is calculated as $I_{MaxPot} = V_{MaxPot}/R_{MaxPot}$.

2.1.1 *Material selection*

The materials to be selected are the substrate, first contact or TCO, *n*- and *p*-type semiconductors, and second contact metal. Because the substrate supports the other materials, it must be highly transparent, physically resistant, chemically stable, and relatively inexpensive; soda-lime glass is the most commonly used commercial material. The most commonly used commercial TCOs are ZnO and ITO. The material characteristics that must be considered to select the *n*- and *p*-type semiconductors are wavelength sensitivity (which is defined by the bandgap), the capacity to absorb incident spectra, and the direct and indirect band-to-band charge transition. For special cases, the material dispensability and cost must also be considered.

2.1.2 *p–n junction structure*

The window and active layer materials must be selected before defining the *p–n* junction structure. The window layer material must have a larger bandgap with better photoconductivity, higher transmittance and lower absorbance to incident spectra, and higher concentration with lower carrier recombination than the active layer material. Meanwhile, the active layer material must have a long lifetime of minority charges so that charges can be collected before they recombine. Once the window and active layer materials are selected, the doping concentrations are defined. If the *p*-type material has a higher doping concentration than the *n*-type material, then the

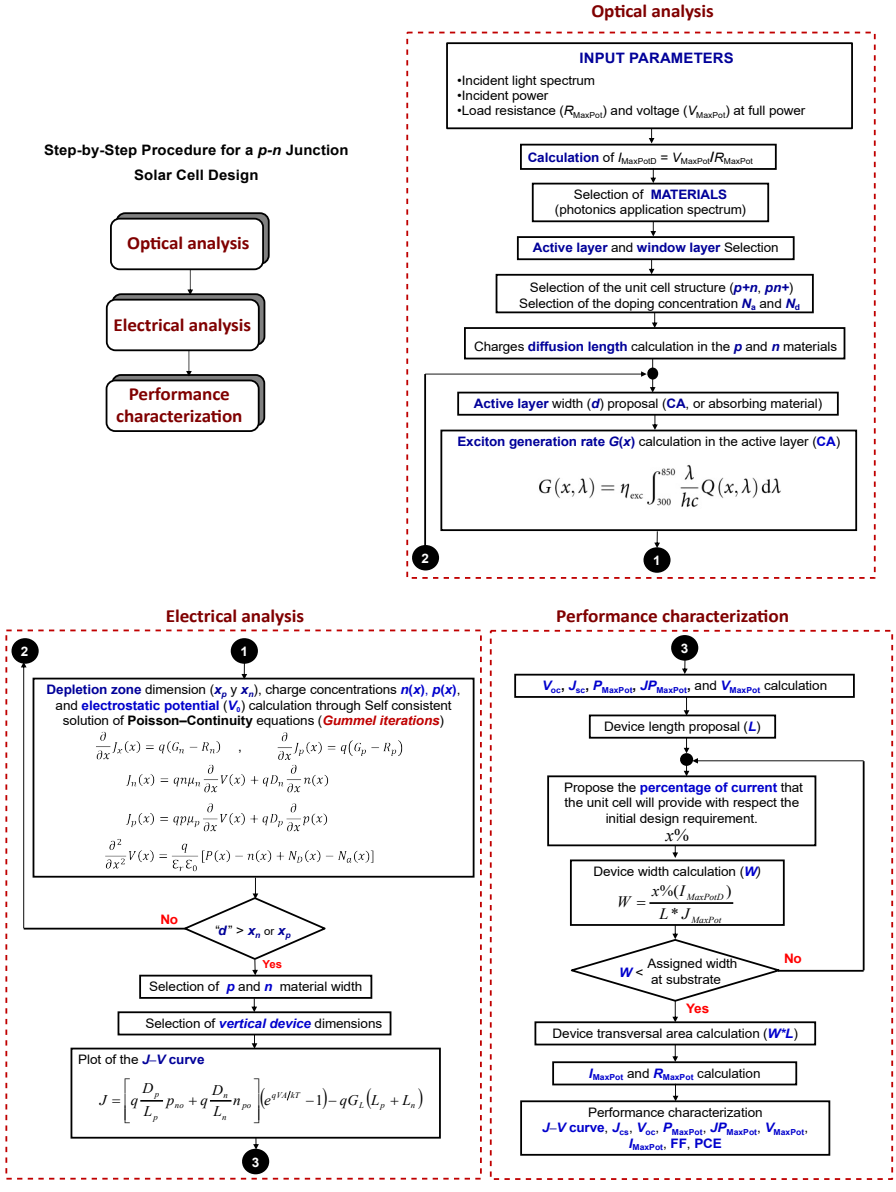

Figure 2 Block diagram containing the step-by-step procedure to design a PV device.

p–n structure is p^+–n; otherwise, it is p–n^+.

2.1.3 *Extraction of G(x, λ)*

Before obtaining $G(x, \lambda)$, the charge diffusion lengths for electrons in the p-type material and holes in the n-type material are calculated using $L_p = \sqrt{\tau_p D_p}$ and, $L_n = \sqrt{\tau_n D_n}$, respectively, where τ_p and τ_n denote the hole and electron lifetimes, respectively, and D_p and D_n denotes the corresponding diffusion coefficients. An initial value for the active layer width (d) is then set. $G(x, \lambda)$ depends on the optical absorption and electromagnetic field distribution in a multi-thin-layer device. One-dimensional transfer matrix theory is used to estimate $G(x, \lambda)$ inside the active layer[22,23]. This theory is based on the Fresnel coefficients calculated under the assumptions that layers constituting a device are homogeneous and isotropic, interfaces are parallel and flat, and incident light is a plane wave normal to the substrate interface. Figure 3 shows the PV device as a stack of thin layers embedded between an ambient and a metallic contact. Because the glass substrate is much thicker than the light coherent length, light transmission through it should not be calculated based on wave interference, but rather by considering the reflection and transmission rates. Each layer is described by its complex refraction index, $\tilde{n}(\lambda) = \overline{n}(\lambda) + i\overline{k}(\lambda)$, which is a function of λ. The optical electric field at any point of the PV device is a complex quantity with a positive index E^+ for waves traveling from left to right and a negative index E^- for waves traveling from right to left. 2 × 2 matrices containing the complex Fresnel reflection (r_{jk}) and transmission (t_{jk}) coefficients, given by Eq. 1, are used to describe the light behavior at the interface between two layers and the propagation through any layer:

$$\boldsymbol{I}_{jk} = \frac{1}{t_{jk}}\begin{bmatrix} 1 & r_{jk} \\ r_{jk} & 1 \end{bmatrix}, \boldsymbol{P}_j = \begin{bmatrix} e^{-i\xi_j d_j} & 0 \\ 0 & e^{i\xi_j d_j} \end{bmatrix} \quad (1)$$

where $\xi_j = 2\pi\tilde{n}_j/\lambda$, with λ as the light wavelength; M_j' and M_j'' are the products of all the interface and propagation matrices before and after the active layer, respectively. The

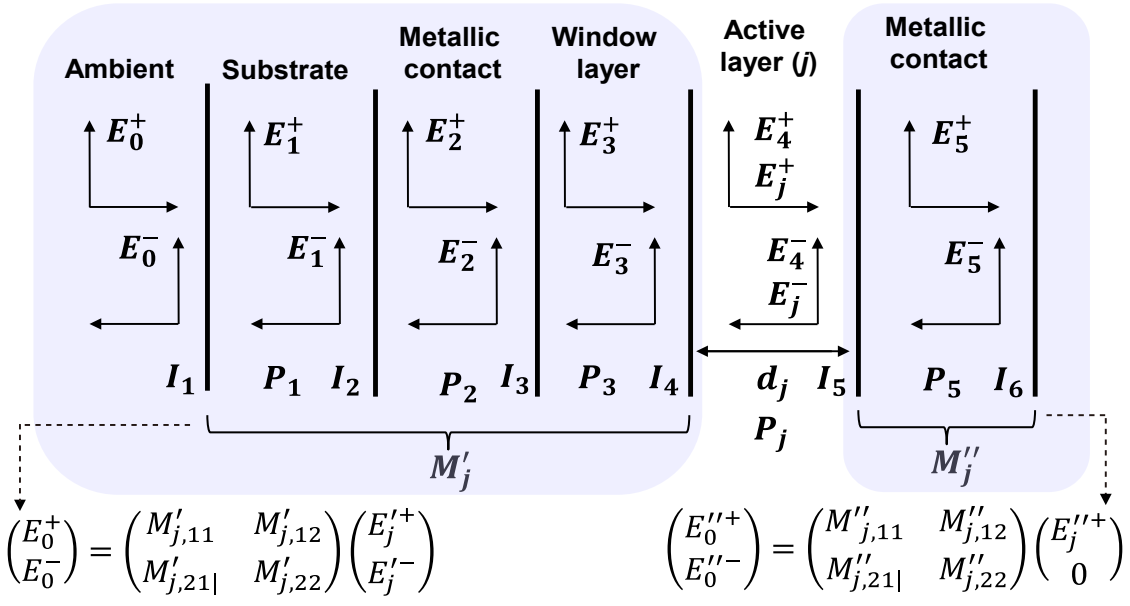

Figure 3 A PV device as a stack of thin layers embedded between an ambient and a metallic contact.

matrices have their own reflection and transmission coefficients, given by $t''_j = 1/M''_{j,11}$, $t'_j = 1/M'_{j,11}$, and $r''_j = M''_{j,21}/M''_{j,11}$, and $r'_j = 1/M''_{j,11}$. Combining the coefficients and considering that the electric field at any point is the sum of the components with positive and negative indices, $E_j(x) = E_j^+(x) + E_j^-(x)$, the total electric field at a point of layer j at distance x from the right side of the interface $(j-1)$ is obtained in terms of the incident field E_0^+ as follows:

$$E_j(x) = t_j^+ \left[e^{i\tilde{\nu}_j x} + r''_j e^{i\tilde{\nu}_j(2d_j - x)} \right] E_0^+ \tag{2}$$

where $r'_{j-} = -M'_{j,12}/M'_{j,11}$ and $t_j^+ = E_j^+/E_0^+ = t'_j/(1 - r'_{j-} r''_j e^{2i\tilde{\nu}_j d_j})$.

The energy dissipated in layer j at position x due to the field normal incident is given by

$$Q_j(x,\lambda) = \frac{1}{2} c\varepsilon_0 \alpha_j \tilde{n}_j |E_j(x)|^2 \tag{3}$$

where c is the speed of light, ε_0 denotes the permittivity in free space, and α_j denotes the absorption coefficient given by $\alpha_j = 4\pi k_j/\lambda$, with k_j as the extinction coefficient of layer j. Thus, the number of excited states is proportional to the number of absorbed photons; hence, $|E|^2$ versus position x in a shell represents the production of excited states at each point. Once Q_j is calculated, and assuming a 100% photon–exciton conversion efficiency of η_{exc}, $G(x, \lambda)$ can be obtained by dividing Q_j by the photon energy of λ. Integrating over all wavelengths of the incident spectrum results in Eq. 4:

$$G(x,\lambda) = \eta_{exc} \int_{300}^{850} \frac{\lambda}{hc} Q(x,\lambda)\, d\lambda \tag{4}$$

where h is Planck's constant. The integration is generally performed from 300 to 850 nm, which is a typical absorbance range of active layers in PV devices.

2.2 Electrical analysis (modeling and Gummel iteration)

The electrical analysis includes the calculations of charge concentration, electrostatic potential, and depletion zone dimensions of the p–n junction under illumination. These parameters are determined by a self-consistent solution of Poisson (Eq. 5) and charge continuity equations (Eqs. 6 and 7)[24–31]. To obtain a self-consistent solution, an initial guess value of the electrostatic potential is required; the charge densities are obtained by solving the charge continuity equations. Then, a corrected electrostatic potential value is calculated using the Poisson equation. The new electrostatic potential is used to update the charge densities. This process is repeated until the convergence criteria are satisfied.

$$\frac{\partial^2}{\partial x^2} V(x) = \frac{q}{\varepsilon_r \varepsilon_0} [n(x) - p(x)] \tag{5}$$

$$\frac{\partial}{\partial x} J_n(x) = qU(x) \tag{6}$$

$$\frac{\partial}{\partial x} J_p(x) = qU(x) \tag{7}$$

where $V(x)$ denotes the electrostatic potential; q denotes the electron charge, $n(x)$ and $p(x)$ denote the electron and hole concentrations, respectively; $J_n(x)$ and $J_p(x)$ denote the electron and hole current densities, respectively; ε_r denotes the dielectric constant; and $U(x)$ denotes the free charge generation rate. To solve the above system of equations, current densities, charge concentrations, and electric potential must be related. These are incorporated in Eqs. 8 and 9, which are the charge current diffusion and drift equations, respectively.

$$J_n = qn\mu_n \frac{\partial}{\partial x} V(x) + qD_n \frac{\partial}{\partial x} n \tag{8}$$

$$J_p = qp\mu_p \frac{\partial}{\partial x} V(x) + qD_p \frac{\partial}{\partial x} p \tag{9}$$

where $D_{n,p} = \mu_{n,p} V_t$ denote the charge diffusion coeffi-

cients, with $V_t = k_B T/q$ as the thermal voltage; k_B as the Boltzmann constant; and T as the absolute temperature.

2.3 Criteria to assign doping concentration, layer thickness, and depletion zone width

Light and moderate doping levels for *n*- and *p*-type semiconductors range from 10^{15} to 10^{17} cm^{-3} whereas high doping levels are $>10^{18}$. In a *p*–*n* junction-based PV device, the window layer material must be doped higher than the active layer material. This higher doping is desired to enlarge the depletion zone in the active layer to accumulate more ionized charges and enhance photon absorption. Referring to layer thickness, the active layer width must be larger than its depletion zone and smaller than its charge diffusion length to make the most of the ionized charges in the depletion zone and avoid wasting material. The window layer width must be smaller than its charge diffusion but not so thin as to prevent a short circuit. The widths of the substrate and the first and second contact layers are normally imposed by the fabrication technique used.

Once the depletion zone dimensions are obtained, consistency of the proposed active layer width is proved by checking whether the d value satisfies the described criterion (greater than the depletion zone but less than the charge diffusion). If this criterion is not satisfied, a new d value is guessed, and the process is repeated until consistency is satisfied.

2.4 Performance metrics

The performance characterization parameters are V_{oc}, J_{sc}, FF, and PCE. V_{oc} and J_{sc} are obtained using Eqs. 10 and 11, respectively, with kT = 0.025 eV, q = 1.602×10^{-19} C, where D_n, L_n, L_p, $G(x, \lambda)$, n_{p0}, and P_{n0} depend on the material and are obtained using the previously described procedures.

$$V_{oc} = \frac{kT}{q} \ln\left[\frac{qG_L(L_p + L_n)}{q\left(\frac{D_p}{L_p}P_{n0} + \frac{D_n}{L_n}n_{p0}\right)} + 1\right] \tag{10}$$

$$J_{sc} = -qG_L(L_p + L_n) \tag{11}$$

To obtain FF and PCE, the *J*–*V* curve must be plotted using Eq. 12. The intersections of the *J*–*V* curve in the *V* and *J* axes are V_{oc} and J_{sc}, respectively. *V* times *J* at each point of the *J*–*V* curve gives the power density curve. The intersection of a line from the point where the maximum power density occurs to the *V* axis gives the maximum power voltage (V_{MaxPot}), and the intersection of a line from the maximum power density to the *J* axis gives the maximum power density current (J_{MaxPot})

$$J = \left(q\frac{D_p}{L_p}P_{n0} + q\frac{D_n}{L_n}n_{p0}\right)e^{\frac{qV}{kT}-1} - qG_L(L_p + L_n) \tag{12}$$

In a practical fabrication, a specific transversal area (A) is assigned for each PV device. If the substrate area is greater than A, an array of PV devices can be fabricated on the same substrate. The assigned transversal area is given by $L_{max}W_{max}$, where L_{max} and W_{max} are the maximum device length and width, respectively. By fixing L_{max}, W_r is calculated using Eq. 13. Because J_{MaxPot} and I_{MaxPot} have been previously obtained, a value for the percentage of the desired current (%I_{MaxPot}) is guessed, and W_r is calculated. The calculated W_r is checked to be close but less than W_{max}. If this condition is not satisfied, a new %I_{MaxPot} is guessed. Once the condition is satisfied, the real device transverse area $A_r = L_{max}W_r$ is calculated, and the resulting %I_{MaxPot} is the percentage of the desired current obtained from a PV device of area A_r. The %I_{MaxPot} is then used to determine the number of PV devices that will be connected in parallel to obtain 100% of I_{MaxPot}.

$$W_r = \frac{x\%I_{MaxPot}}{LJ_{MaxPot}} \tag{13}$$

Once the device width (W) and length (L) are obtained, the transverse area can be obtained. Thus, the current at maximum power (I_{MaxPot}) is obtained using Eq. 14:

$$I_{MaxPot} = J_{MaxPot}A \tag{14}$$

Equation 15 is used to obtain FF based on the previously obtained V_{MaxPot}, I_{MaxPot}, V_{oc}, and I_{sc}:

$$FF = \frac{V_{MaxPot}I_{MaxPot}}{V_{oc}I_{sc}} \tag{15}$$

Equations 16–18 are used to calculate PCE, P_{MaxPot}, and R_{MaxPot}, respectively.

$$PCE = \frac{V_{MaxPot}J_{MaxPot}}{P_{incidente}} \tag{16}$$

$$R_{MaxPot} = \frac{V_{MaxPot}}{I_{MaxPot}} \tag{17}$$

$$P_{MaxPot} = JP_{MaxPot}A \tag{18}$$

3 Theoretical design results

A single *p*–*n* CdS/CdTe heterojunction PV device was theoretically designed using the proposed step-by-step procedure. The design was realized under Shockley–Queisser (SQ) conditions (the only loss mechanism is radiative recombination; ideal contact electrodes; and SQ-limit for CdTe-based PV device ≈ 29%) [32]. The input parameters are incident light spectra from 300 to 850 nm, a 1000 W/m^2 average optical power (AM1.5G), a 50 Ω load resistance, and 5 V voltage to be delivered by the PV device at maximum power. Table 1 lists the material properties and constant parameter values used in calculations. $I_{MaxPotD}$ = 100 mA was obtained. The selected *p*- and *n*-type materials are CdTe and CdS, respectively, with 1.42 and 1.5 eV bandgaps, respectively. To make the depletion zone of the active layer wider, CdS has a higher doping concentration than CdTe, resulting a *p*–n^+ structure. L_p and L_n were then calculated.

Using the material complex refraction index presented in Appendix, for an initial active layer width of d = 10 μm, $E(x, \lambda)$, $Q(x, \lambda)$, and $G(x, \lambda)$ were obtained for the considered wavelength range using Eqs. 4–6, respectively. Figure 4a shows the normalized modulus squared of the optical electric field distribution in the active layer versus active layer depth versus wavelength. From the figure, a high optical electric field is concentrated in the wave-

Table 1 Typical values used in calculations

Parameter	Symbol	Value	Ref.
Planck constant (eV·s) ($m^2 \cdot kg \cdot s^{-1}$)	h	$4.13566733 \times 10^{-15}$ 6.63×10^{-34}	[33, 34]
Dirac constant ($m^2 \cdot kg \cdot s^{-1}$)	$\hbar$	6.582118×10^{-16}	
Boltzmann constant (eV)	k_B	8.617×10^{-5}	
Free electron mass in vacuum (kg)	m_0	9.1093×10^{-31}	
Vacuum permittivity ($C^2 \cdot N^{-1} \cdot cm^{-2}$)	ε_0	8.854×10^{-12}	
Speed of light ($m \cdot s^{-1}$)	c	299792458	
Electron charge (C)	q	1.6×10^{-19}	
Intraband scattering time (s)	τ_n	1×10^{-12}	
***n*-type CdS**			
Dielectric constant	$\varepsilon_{r,CdS}$	$10\varepsilon_0$	
Bandgap (eV, at 300 K)	$B_{g,CdS}$	2.42	
Electron effective-mass (kg)	m_{en}	$0.21m_0$	
Hole effective-mass (kg)	m_{hn}	$0.8m_0$	
Electron mobility ($cm^2 \cdot V^{-1} \cdot s^{-1}$)	$\mu_{e,CdS}$	200	[35–37]
Hole mobility ($cm^2 \cdot V^{-1} \cdot s^{-1}$)	$\mu_{h,CdS}$	10	
Hole diffusion coefficient ($cm^2 \cdot s^{-1}$)	D_p	0.26	
Intrinsic concentration (cm^{-3})	$n_{i,CdS}$	1×10^{-2}	
Electron life time (s)	τ_e	1×10^{-10}	
***p*-type CdTe**			
Dielectric constant	$\varepsilon_{r,CdTe}$	$10.5\varepsilon_0$	
Bandgap (eV, at 300 K)	$B_{g,CdTe}$	1.5	
Electron effective-mass (kg)	m_{ep}	$0.11m_0$	
Hole effective-mass (kg)	m_{pp}	$0.4m_0$	
Electron mobility ($cm^2 \cdot V^{-1} \cdot s^{-1}$)	$\mu_{e,CdTe}$	320	[37–39]
Hole mobility ($cm^2 \cdot V^{-1} \cdot s^{-1}$)	$\mu_{h,CdTe}$	40	
Electron diffusion coefficient ($cm^2 \cdot s^{-1}$)	D_n	7.8	
Intrinsic concentration (cm^{-3})	$n_{i,CdTe}$	5.1×10^5	
Hole life time (s)	τ_p	1×10^{-10}	

length range of 550–750 nm, consistent with the irradiated solar spectra considered in the AM1.5G standard Fig. 4b shows the time average energy dissipated per second in the active layer at normal incidence versus active layer depth versus active layer wavelength. From the figure, a high dissipation field is concentrated at different positions of the 3D plot. Energy dissipation peaks are observed at depths of 1–2 and 4–5 μm. The peak positions are consistent with the peak positions for the optical electric field distribution because high field dissipation occurs where high electric fields exist. Figure 4c shows the exciton generation profile versus active layer depth versus active layer wavelength. From the figure, high exciton generation is obtained at the areas where high dissipation fields are concentrated. This result is expected because high dissipation is attributed to high field absorption. The active layer width at which $G(x, \lambda)$ is the maximum is known as the optimal active layer width. Figure 5 shows a plot of $G(x, \lambda)$ versus active layer width. From the figure, the maximum $G(x, \lambda)$ (3.7172×10^{29} nm^{-3} s^{-1}) is obtained at 8.5 μm, and insignificant changes are observed beyond this value. Hence, the active layer width of 8.5 μm optimizes the material and maximizes the exciton generation.

The Poisson and charge continuity equations (Eqs. 5, 8, and 9) are self-consistently solved to determine the charge concentrations ($n(x)$ and $p(x)$), electrostatic potential ($V_{poisson}$), and depletion zone dimensions of the p–n junction under optical stimulation. Figure 6 shows the iterative algorithm used to obtain the self-consistent solution (Gummel iterations). The algorithm is initiated by calculating the charge diffusion length and charge concentrations at thermal equilibrium. Then, with a guessed $V_{poisson}$ of 0.6 V, based on the solution of the Poisson equation in the p–n junction and Anderson theory, x_p, x_n, $n(x)$, $p(x)$, and a new $V_{poisson}$ are obtained. Next convergence criteria $(V_{i,poisson} - V_{i-1,poisson}) \leq \varepsilon_1$ and $[|\Delta n(x)| - |\Delta p(x)|] / (n_i + p_i) \leq \varepsilon_2$ are verified, where $\varepsilon_1 = 0.1$ and $\varepsilon_2 = 0.01$ are predefined threshold values. The typical number of Gummel iterations for the used materials is <100, depending on doping concentrations (N_a and N_d). In this study, the algorithm converges at 21 iterations. Table 2 summarizes the results obtained from applying the iterative algorithms for the self-consistent solution of the Poisson and charge continuity equations. The diffusion electron and hole distances are less than 1 μm when the depletion zone width is 8.351×10^{-5} cm. The active layer has a wider depletion zone (x_n), attributable to the higher doping concentration at the CdS window layer. In addition, a greater charge concentration is observed at the active layer, mainly due to the wider depletion zone. An electrostatic potential $V_{poisson}$ = 0.6006 V was found at the depletion zone, which is around the typical value for semiconductor materials.

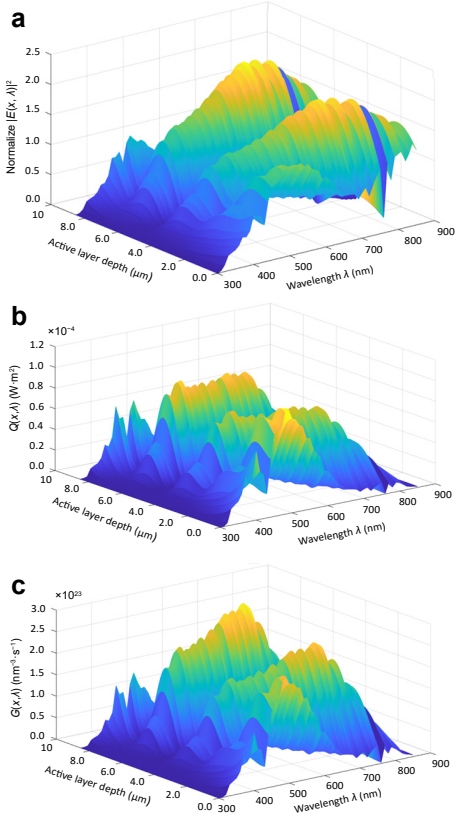

Figure 4 Field distribution in the CdTe layer. (a) Optical electrical field $|E|^2$. (b) Dissipation field $Q(x, \lambda)$. (c) Exciton generation field $G(x, \lambda)$.

Consistency of the optimized active layer width is satisfied because 8.5 μm is greater than the depletion zone's length $(x_n = 1.6699 \times 10^{-8}$ cm). The window layer width was set to 100 nm, which is less than the charge diffusion length in this layer, but not so thin as to prevent a short circuit. The widths of the substrate and the first and second contact layers are imposed by the fabrication technique to be 1.1 mm, 200 nm, and 5 μm, respectively. Figure 7a shows the designed PV device, including the structure, material selection, layer dimensions, and doping concentrations. Figure 7b shows the obtained performance characterization parameters. V_{oc} and J_{sc} were calculated using Eqs. 10 and 11, respectively, with $kT = 0.025$ eV, $q = 1.602 \times 10^{-19}$ C, $D_n = 7.8$ cm^2/s, and L_n, L_p, $G(x,\lambda)$, n_{p0}, and p_{n0} obtained using the previously described procedures. Then, the J–V curve was plotted using Eq. 12. From the J–V curve, V_{MaxPot}, J_{MaxPot}, FF, and PCE were obtained. An area of 4 × 4 mm^2 was assigned for a single PV device. A full-size value of L = 4 mm was assigned, and W = 3.99 mm was obtained using Eq. 13 with x% = 0.07. A transverse area of A_{transv} = 15.96 mm^2 was obtained using Eq. 14. FF = 88.54% was obtained using Eq. 15, PCE = 28.64% was obtained using Eq. 16, and R_{MaxPot} = 1.5 kΩ and P_{MaxPot} = 4.575 mW were obtained using Eqs. 17 and 18, respectively. Considering SQ conditions in the theoretical design, the obtained PCE = 28.64% is close to the reported SQ-limit (≈ 29 %) for B_g = 1.5 eV [40] and more accurate than the recently reported theoretical efficiencies for CdTe-based PV devices; for example, PCE = 27.35% and 20.94% were

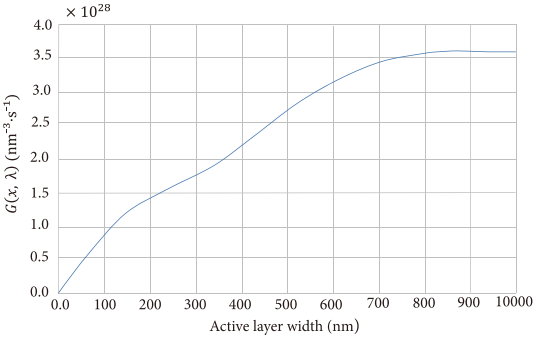

Figure 5 Plot of $G(x, \lambda)$ versus CdTe layer width.

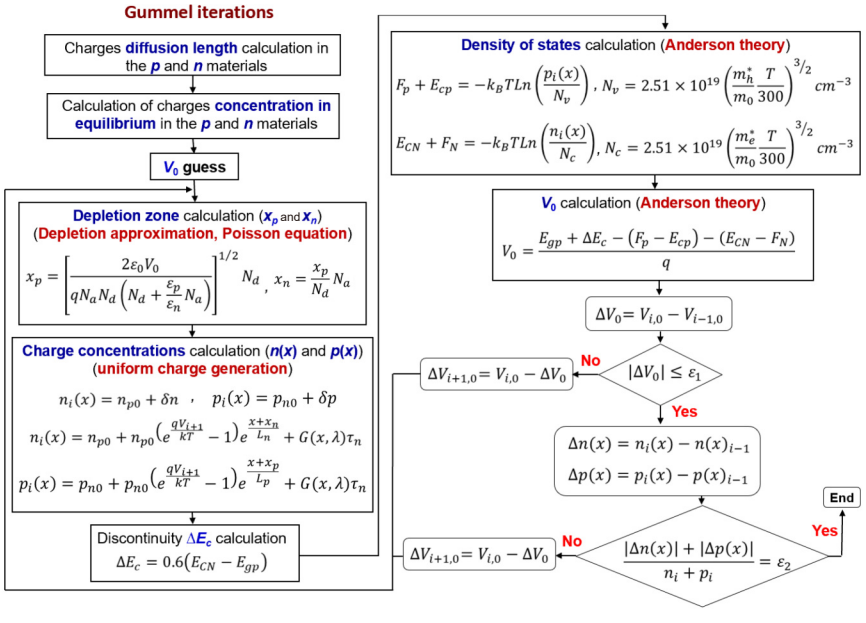

Figure 6 Iterative algorithms for the self-consistent solution of Poisson and charge continuity equations.

Table 2 Results obtained from applying iterative algorithms for the self-consistent solution of Poisson and charge continuity equations.

Parameter	CdS (*n*-type)		CdTe (*p*-type)
Diffusion charge distance (cm)	$L_n = 2.7928 \times 10^{-5}$		$L_p = 5.099 \times 10^{-6}$
Minority charge concentration at equilibrium (cm^{-3})	$n_{p0} = 2.601 \times 10^{-6}$		$p_{n0} = 2.00 \times 10^{-25}$
Depletion zone (cm)	$x_p = 8.3493 \times 10^{-5}$		$x_n = 1.6699 \times 10^{-8}$
Donor concentration (cm^{-3})		$N_d = 5 \times 10^{20}$	
Acceptor concentration (cm^{-3})		$N_a = 1 \times 10^{17}$	
Charge concentration (cm^{-3})	$p_i(x) = 5.9003 \times 10^{11}$		$n_i(x) = 3.7172 \times 10^{12}$
Quasi–Fermi levels (eV)	$F_p - E_{cp} = 0.4402$		$E_{CN} - F_N = 0.3854$
Electrostatic potential (V)		$V_{poisson} = 0.6006$	
Contact potential (V)		$V_{contact} = 1.2264$	

obtained using SCAPS-1D simulation [41,42] and PCE = 28.36% was obtained by optimizing the thickness and doping concentration [43]. Figure 7d shows the PCE, V_{oc}, J_{sc}, and FF parameters versus d in the range of 1–10 μm; also, $G(x,\lambda)$ is related in the figure. The optimal performance was obtained at a width d = 8.5 μm. Below this value, all parameters decrease with the width; above it, they decrease with a slower slope. This behavior is attributed to $G(x,\lambda)$ because it also increases with d (Fig. 5).

4 Practical implementation

To fabricate a glass/ITO/CdS/CdTe/Ag PV device, a 50×50×1.1 mm^3 transparent soda-lime glass coated with a 200 nm ITO layer was obtained from Techinstro (Fig. 8a). A three-electrode electrodeposition setup with a platinum foil as the counter electrode was used to deposit successive thin films [44]. The fabrication procedure includes substrate and electrode cleaning, electrolyte preparation, power source connection, and thin film deposition. To electrodeposit each semiconductor, the electrolyte was prepared using different chemical reagents and working conditions. Ethylene glycol (EG 99%, from Sigma-Aldrich) was used as a supporting electrolyte in all solutions. First, the soda-lime glass substrate coated with ITO was cleaned in an ultrasonic bath containing acetone and isopropyl alcohol, each for 300 s, followed by drying at room temperature. The solution for CdS electrodeposition was prepared using

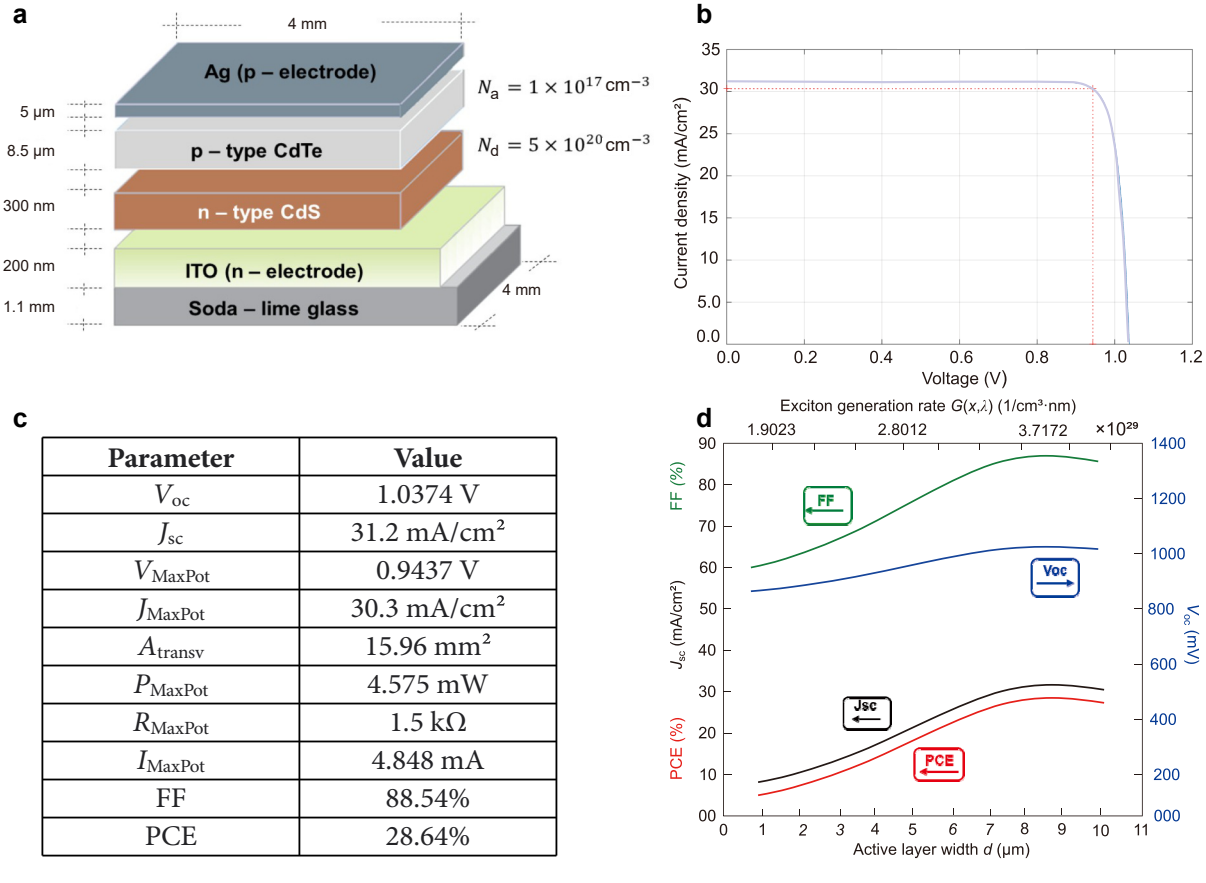

Parameter	Value
V_{oc}	1.0374 V
J_{sc}	31.2 mA/cm²
V_{MaxPot}	0.9437 V
J_{MaxPot}	30.3 mA/cm²
A_{transv}	15.96 mm²
P_{MaxPot}	4.575 mW
R_{MaxPot}	1.5 kΩ
I_{MaxPot}	4.848 mA
FF	88.54%
PCE	28.64%

Figure 7 Designed PV device. (a) Device structure, materials selection, layer dimensions, and doping concentrations; (b) Performance characterization.

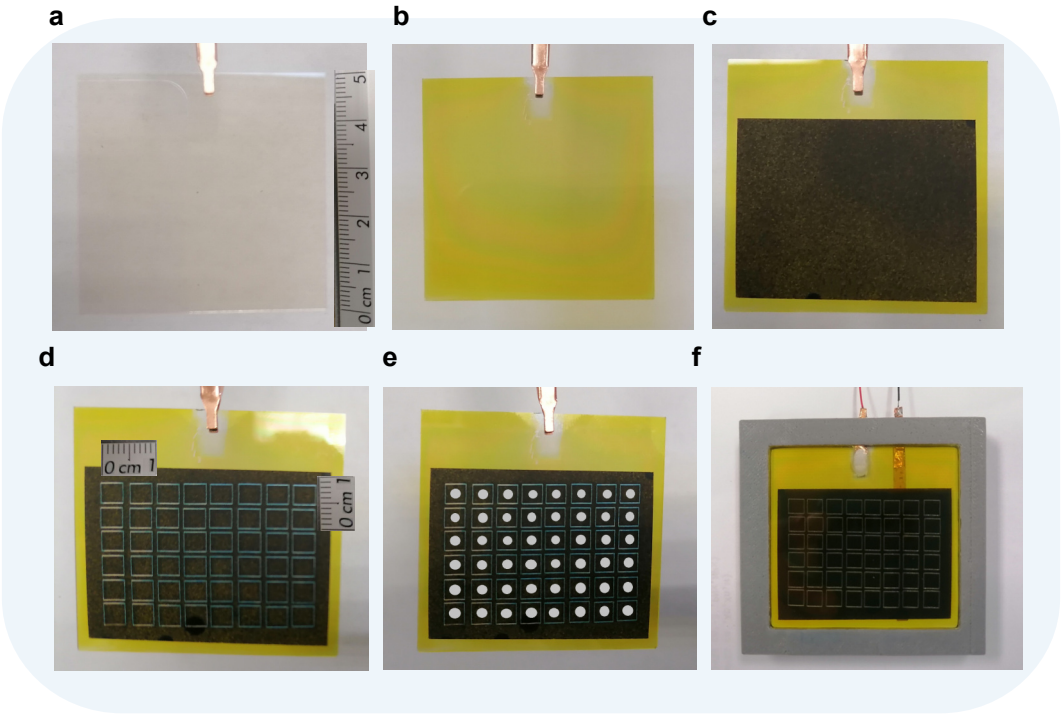

Figure 8 PV device fabrication. (a) 50×50×1.1 mm³ transparent soda-lime glass coated with a 200 nm ITO layer; (b) electrodeposited CdS thin film; (c) electrodeposited CdTe thin film; (d) segmented PV devices; (f) metalized PV devices; (f) tested PV device array.

150 mL of EG, 0.036 mol of cadmium chloride ($CdCl_2$ 99%), and 0.102 mol of sulfur (S 99%). All reagents were mixed using a magnetic stirrer on a hot plate at 40°C until a homogeneous solution was obtained. Then, the temperature was increased to 140°C. The electrodeposition time was 35 min with a constant current density of 15 mA/cm² at 140°C. Subsequently, the substrate containing the electrodeposited CdS film was ultrasonically cleaned in isopropyl alcohol for 60 s to eliminate any remaining residue. Figure 8b shows the substrate with the electrodeposited CdS film after the post-electrodeposition ultrasonic cleaning process. CdTe was deposited on the coated glass/ITO/CdS substrate. The electrolyte solution was prepared using 150 mL of EG, 1 mol of $CdCl_2$, 0.160 mol of potassium iodide (KI 99%), and 0.010 mol of tellurium chloride ($TeCl_4$ 99%) in a magnetic stirrer on a hot plate at 40°C to ensure a homogeneous solution. Then, the temperature was increased to 90°C. The electrodeposition time was 20 min, maintaining a constant current density and temperature of 2.5 mA/cm² and 90°C, respectively. Further, the complete arrangement was heated for 300 s at 180°C to enhance the adhesion between the formed films. Figure 8c shows the substrate with the electrodeposited CdTe film after the post-electrodeposition.

As shown in Fig. 8d, an array of 48 PV devices was segmented on the deposited films. The segmentation was realized using an engraving laser machine model iCube Pro 3W from Sculpfun. Each PV device has a length and width of 4 mm. The second contact layers were added by dropping conductive Ag paste on top of each PV device (Fig. 8e). Figure 8f shows the fabricated PV device array. The PV device array was characterized using a Keithley meter system coupled with a 1,000 W/m² xenon lamp. The characterized wavelength range was 300–850 nm. Figure 9a shows the obtained *J*–*V* curve and the measured

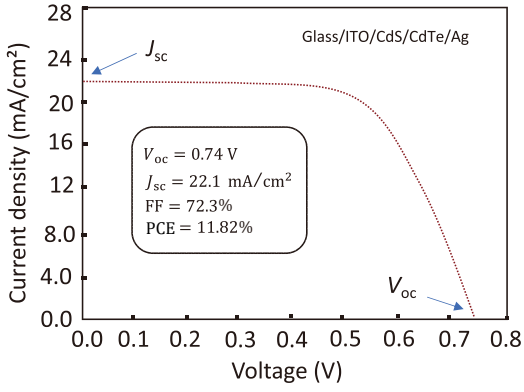

Figure 9 Obtained *J*–*V* curve and measured characterization parameters.

characterization parameter. V_{oc} = 0.74 V, J_{sc} = 22.1 mA/cm², FF = 72.3 %, and PCE = 11.82% were obtained from measurements. The measured PCE obtained via electrodeposition as a manufacturing technique is 16.82% less than that obtained in the theoretical design and approximately 50% less than those recently reported for CdTe-based PV devices, e.g., PCE = 22.0%–22.3% with V_{oc} = 870–917 mV, FF = 78%–80%, and J_{sc} = 30–32 mA/cm²[45–48]. Hence, the obtained PCE difference between the measurement and theoretical design is used to correlate $G(x,\lambda)$ in the next section.

5 Theoretical and practical result correlation

The theoretical calculations yield betterm performance than the practical measurements for the single *p*–*n* junction PV device, attributable to ideal internal efficiencies

considered under SQ conditions assumed in theoretical design, e.g., ideal optical losses where each photon impacting a cell is absorbed (η_{abs}). The losses occur because not all incoming light is absorbed and can include reflection, transmission, absorption losses in the non-active layers, shading losses, spectral mismatch, and scattering losses. In addition, ideal nonradiative recombination, where each absorbed photon generates an exciton (η_{exc}), can occur. These losses occur in semiconductors, where an electron and a hole recombine or disappear without producing an exciton or a new photon for reabsorption, losing their energy as heat (phonons). The losses can include Shockley–Read–Hall, Auger, and surface recombinations. Further, ideal exciton dissociation (η_{fr}), where each bound electron–hole pair separates, can generate free charges in the contact electrodes. Such losses can include imperfect charge separation and bandgap mismatch. Ideal contact losses, where each free charge at the electrodes is collected (η_{cc}), can also occur. Such losses can include high contact resistance, shunt resistance, poor surface passivation, and poor contact area and grid design.

The associated losses that affect the performance characterization parameters of PV devices are not accounted for in ideal η_{abs}, η_{exc}, η_{fr}, and η_{cc}. For example, optical losses reduce the amount of light that can be absorbed and directly affect J_{sc} and hence PCE[49]. Nonradiative recombination directly reduces the number of charge carriers available for current generation, resulting in lower PCE, reduced V_{oc}, and reduced FF, thereby reducing the overall performance[50]. Dissociation losses reduce V_{oc} and FF because they reduce the number of usable charge carriers, also leading to poor photocurrent generation, which is a major contributor to reduced PCE[51]. Contact losses lead to lower FF, which is the primary indicator of how efficiently a PV device can deliver power, and its main impact will be visible as a reduction in the J–V curve slope near V_{oc}, causing a flattening of the curve in the high-current region[52]. Because η_{abs}, η_{exc}, η_{fr}, and η_{cc} depend on the materials and fabrication technique, theoretical efficiencies are tuned to adjust measurements with calculations. Then, the tuned values are used as fixed quantities for that particular fabrication technique and materials. In this work, the theoretical PCE is 16.82% higher than the practical PCE. To adjust PCE, Fig. 10, which shows a plot of PCE versus $G(x,\lambda)$ for different doping ratios ($\Delta D = N_a/N_d$), is used for correlation. Using the expanded plots of Fig. 10b for a doping ratio of $\Delta D = 0.0002$, a theoretical PCE of 28.64% is obtained with a theoretical $G(x,\lambda)$ of 3.7172×10^{29} nm^{-3} s^{-1} whereas a PCE of 11.82% is obtained from measurement with a $G(x,\lambda)$ of 1.5240×10^{29} nm^{-3} s^{-1}. This means that only 41.27% of absorbed photon generates an exciton ($\eta_{exc} = 0.4127$). Notably, the loss mechanism not included in η_{exc} may be included to correlate and adjust η_{abs}, η_{fr}, and η_{cc}, or a combination of them.

6 Conclusion

In this study, a step-by-step procedure for PV device design was proposed. The proposed procedure comprises three main processes: 1) an optical analysis to determine the exciton generation rate in the active device region, 2) an electrical analysis to determine the charge concentrations, electrostatic potential, and depletion zone dimensions of the p–n junction under optical stimulation, and 3) the performance characterization parameters, including V_{oc}, J_{sc}, FF, and PCE. Further, progressive electrodeposition of CdS, CdTe, and Ag films on ITO-coated glass was performed to fabricate the designed PV device. Theoretical and practical results for the designed and fabricated CdS/CdTe-based PV device are also presented and discussed. $G(x,\lambda)$ was first used to determine the optimal active layer width and then to correlate the obtained theoretical calculations with practical measurements. Because performance differences between theoretical calculations and practical measurements are attributed to ideal considerations in the theoretical design, for example, η_{abs}, η_{exc}, and η_{cc} equal to one, and these efficiencies depend on the materials and fabrication technique, they are tuned to adjust measurements with calculations. In this study, only $\eta_{exc} = 0.4127$ value was adjusted for the designed CdS/CdTe PV device and the fabrication technique was electrodeposition. The adjusted value is used to correlate the calculated and measured PCE values. A more detailed correlation can be obtained by adjusting more than one efficiency parameter. The proposed step-by-step procedure can easily be adapted to design different device structures and materials. The findings of this study can help designers and engineers interested in correlating theoreti-

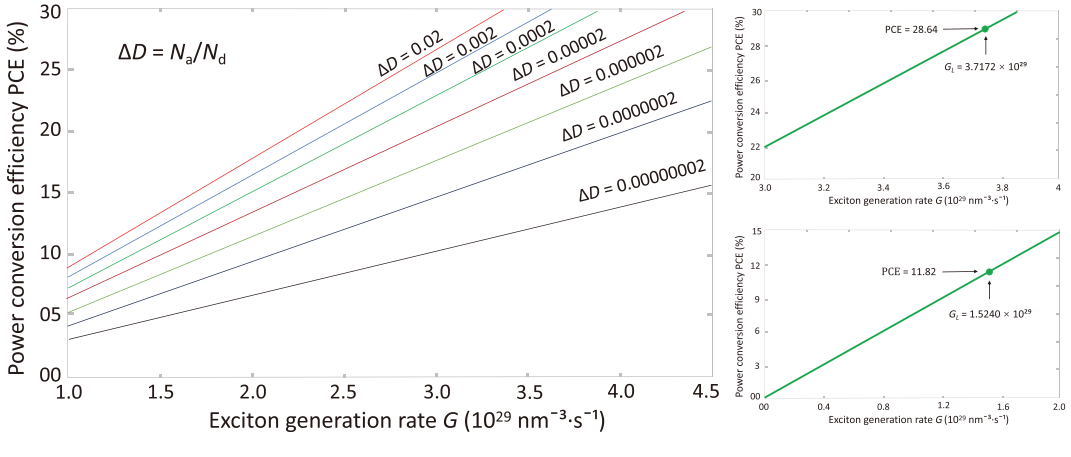

Figure 10 (a) Plots of PCE versus $G(x)$ for different doping ratios ($\Delta D = N_a/N_d$). (b) Expansion for the theoretical PCE of 28.64% and measured PCE of 11.82%.

cal calculations with practical measurements.

Acknowledgements

None.

Author contribution statement

Not applicable.

Data availability

The data that support the findings of this study is available from the corresponding author upon reasonable request.

Declaration of competing interest

The contributing author declares no conflicts of interest exist for this publication.

Funding

This work is granted by Universidad Autónoma de Baja California (Grant No. 111/6/C/26/24).

Use of AI statement

None.

Appendix

Materials complex index of refraction obtained with an ellipsometer EC-400 from J.A. Woollam Co. Inc. for the wavelength range from 300 nm to 850 nm.

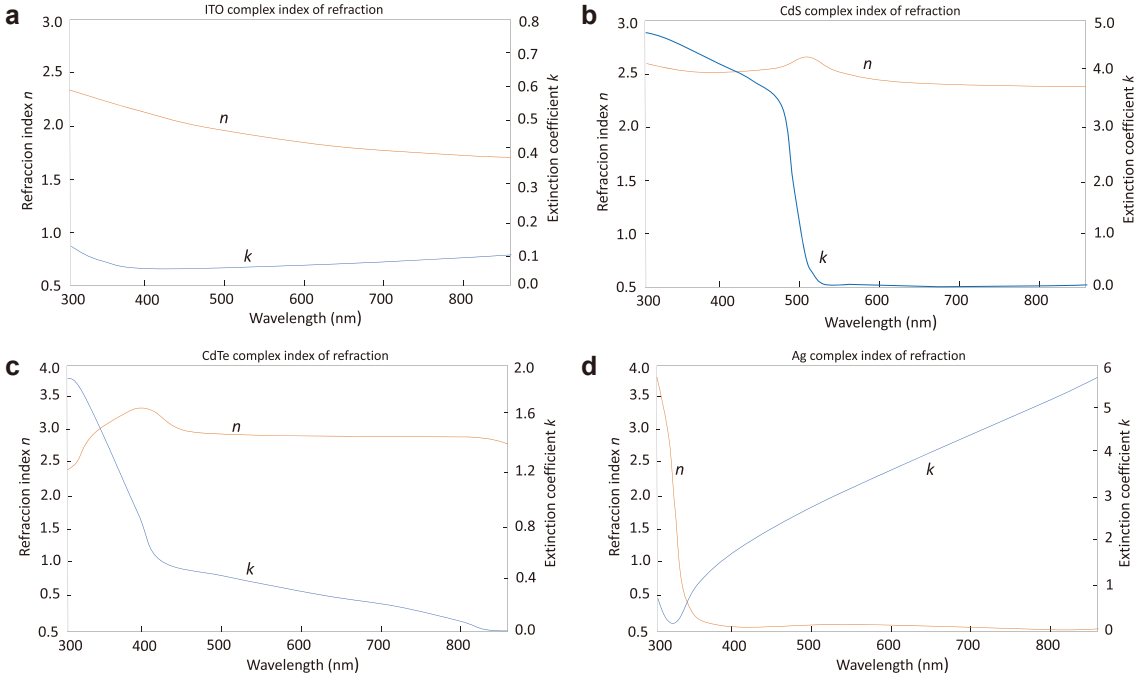

Figure A1 Complex index of refraction of the used materials. (a) ITO, (b) CdS, (c) CdTe, and (d) Ag.

References

[1] Kowsar, A., Debnath, S. C., Shafayet-Ul-Islam, M., Hossain, M. J., Hossain, M., Chowdhury, A. F. M. K., Hashmi, G., Farhad, S. F. U. (2015). An overview of solar cell simulation tools. *Solar Energy Adv.* 5, 100077.

[2] Al-Ezzi, A. S., Ansari, M. N. M. (2022). Photovoltaic solar cells: a review. *Appl. Syst. Innov.* 5, 67.

[3] Marques Lameirinhas, R. A., Torres, J. P. N., de Melo Cunha, J. P. (2022). A photovoltaic technology review: history, fundamentals and applications. *Energies* 15, 1823.

[4] Pastuszak, J., Węgierek, P. (2022). Photovoltaic cell generations and current research directions for their development. *Materials* 15, 5542.

[5] Huang, S. J. (2021). Grand challenges and opportunities in photovoltaic materials and devices. *Front. Photonics* 2, 651766.

[6] Shahsavari, A., Akbari, M. (2018). Potential of solar energy in developing countries for reducing energy-related emissions. *Renew. Sust. Energy Rev.* 90, 275–291.

[7] Maka, A. O. M., Alabid, J. M. (2022). Solar energy technology and its roles in sustainable development. *Clean Energy* 6, 476–483.

[8] Scarpulla, M. A., Mccandless, B., Phillips, A. B., Yan, Y. F., Heben, M. J., Wolden, C., Xiong, G., Metzger, W. K., Mao, D., Krasikov, D., et al. (2023). CdTe-based thin film photovoltaics: recent advances, current challenges and future prospects. *Sol. Energy Mater. Sol. Cells* 255, 112289.

[9] García, I. (2025). Chapter 5 - Silicon solar cell fabrication technology. In *Fundamentals of Solar Cells and Photovoltaic Systems Engineering*. Victoria, M., Ed. London: Academic Press, p 129–171.

[10] Wu, X. Z. (2004). High-efficiency polycrystalline CdTe thin-film solar cells. *Sol. Energy* 77, 803–814.
[11] Kosyachenko, L. A., Savchuk, A. I., Grushko, E. V. (2009). Dependence of efficiency of thin-film CdS/CdTe solar cell on parameters of absorber layer and barrier structure. *Thin Solid Films* 517, 2386–2391.
[12] Jaber, A. Y., Alamri, S. N., Aida, M. S. (2012). CdS thin films growth by ammonia free chemical bath deposition technique. *Thin Solid Films* 520, 3485–3489.
[13] Reyes-Verdugo, L. A., Villa-Angulo, C., Solis-Pomar, F. (2022). Improvement of the optical absorption of a photovoltaic device by embedding an ultra-thin film of $CdSe_xTe_{1-x}$ in its absorber layer. *MRS Commun.* 12, 1250–1255.
[14] Romeo, N., Bosio, A., Canevari, V., Podestà, A. (2004). Recent progress on CdTe/CdS thin film solar cells. *Sol. Energy* 77, 795–801.
[15] Tamayo-Bello, C., Sauceda-Carvajal, Á., Villa-Angulo, R., Villa-Angulo, C. (2022). Photoinstability aversion in perovskite solar cell by downconversion cadmium chalcogenide filters. *J. Photon. Energy* 12, 025501.
[16] Ma, W. W., Xue, X. P., Liu, G. (2018). Techno-economic evaluation for hybrid renewable energy system: application and merits. *Energy* 159, 385–409.
[17] PV Lighthouse (2024). Overview of PV simulation programs. PV Lighthouse [Online]. https://www.pvlighthouse.com.au/simulation-programs.
[18] Haddout, A., Raidou, A., Fahoume, M. (2019). A review on the numerical modeling of CdS/CZTS-based solar cells. *Appl. Phys. A* 125, 124.
[19] Tcheum, G. L. M., Ngoupo, A. T., Ouédraogo, S., Guirdjebaye, N., Ndjaka. J. M. B. (2020). Numerical analysis of ultrathin Cu (In,Ga) Se_2 solar cells with Zn(O,S) buffer layer. *Pramana* 94, 111.
[20] Parajuli, D., Gaudel, G. S., KC, D., Khattri, K. B., Rho, W. Y. (2023). Simulation study of TiO_2 single layer anti-reflection coating for GaAs solar cell. *AIP Adv.* 13, 085002.
[21] Beser, E. (2024). Design and implementation of a new photovoltaic simulator. *Electr. Eng.* 106, 4561–4574.
[22] Aliaghayee, M. (2024). An overview of the numerical modeling, simulation, and optimization methods: toward the design of highly efficient planer perovskite solar cells. *Disc. Electron.* 1, 35.
[23] Heavens, O. S. (1960). Optical properties of thin films. *Rep. Prog. Phys.* 23, 1.
[24] Pettersson, L. A. A., Roman, L. S., Inganäs, O. (1999). Modeling photocurrent action spectra of photovoltaic devices based on organic thin films. *J. Appl. Phys.* 86, 487–496.
[25] Sievers, D. W., Shrotriya, V., Yang, Y. (2006). Modeling optical effects and thickness dependent current in polymer bulk-heterojunction solar cells. *J. Appl. Phys.* 100, 114509.
[26] Kotlarski, J. D., Blom, P. W. M., Koster, L. J. A., Lenes, M., Slooff, L. H. (2008). Combined optical and electrical modeling of polymer: fullerene bulk heterojunction solar cells. *J. Appl. Phys.* 103, 084502.
[27] Koster, L. J. A., Smits, E. C. P., Mihailetchi, V. D., Blom, P. W. M. (2005). Device model for the operation of polymer/fullerene bulk heterojunction solar cells. *Phys. Rev. B* 72, 085205.
[28] Gommans, H. H. P., Kemerink, M., Kramer, J. M., Janssen, R. A. J. (20005). Field and temperature dependence of the photocurrent in polymer/fullerene bulk heterojunction solar cells. *Appl. Phys. Lett.* 87, 122104.
[29] Lacic, S., Inganäs, O. (2005). Modeling electrical transport in blend heterojunction organic solar cells. *J. Appl. Phys.* 97, 124901.
[30] Glatthaar, M., Riede, M., Keegan, N., Sylvester-Hvid, K., Zimmermann, B., Niggemann, M., Hinsch, A., Gombert, A. (2007). Efficiency limiting factors of organic bulk heterojunction solar cells identified by electrical impedance spectroscopy. *Sol. Energy Mater. Sol. Cells* 91, 390–393.
[31] Kirchartz, T., Pieters, B. E., Taretto, K., Rau, U. (2008). Electro-optical modeling of bulk heterojunction solar cells. *J. Appl. Phys.* 104, 094513.
[32] Deibel, C., Baumann, A., Lorrmann, J., Dyakonov, V. (2007). Polaron pair dissociation and polaron recombination in polymer: fullerene solar cells. *MRS Onl. Proc. Libr.* 1031, 921.
[33] Tiesinga, E., Mohr, P. J., Newell, D. B., Taylor, B. N. (2021). CODATA recommended values of the fundamental physical constants: 2018. *J. Phys. Chem. Ref. Data* 50, 033105.
[34] Sturm, S., Köhler, F., Zatorski, J., Wagner, A., Harman, Z., Werth, G., Quint, W., Keitel, C. H., Blaum, K. (2014). High-precision measurement of the atomic mass of the electron. *Nature* 506, 467–470.
[35] Villa-Angulo, C., Sauceda-Carvajal, D., Villa-Angulo, J. R., Villa-Angulo, R. (2016). Optical field dissipation in heterostructures for nanophotovoltaic devices. *J. Nanophoton.* 10, 046001.
[36] Villa-Angulo, C., Guayante-Santacruz, F. J., Villa-Angulo, R., Hernández-Fuentes, I. O., Morales-Carbajal, R., Villa-Angulo, J. R. (2018) Correlation of theory with experimental photon absorption and photon emission of quasitype II CdS/ZnS QDs. *J. Nanophoton*. 12, 046010.
[37] Tarín-Cordero, J. C., Villa-Angulo, R., Villa-Angulo, J. R., Villa-Angulo, C. (2015). Low-dimensional CdS/CdTe multiple-quantum well heterostructure for optical refrigeration. *J. Nanophoton.* 9, 093085.
[38] Villa-Angulo, J. R., Villa-Angulo, R., Villa-Angulo, C. E. (2013). Photon absorption coefficient (α) for a low-dimensional CdS/CdTe absorber by a partial k-selection approach. *J. Nanophonon.* 7, 073099.
[39] Villa-Angulo, J. R., Villa-Angulo, R., Solorio-Ferrales, K., Ahumada-Valdez, S. E., Villa-Angulo, C. (2014). Effect of effective mass mismatch in CdS/CdTe heterojunctions on the fundamental design parameters of nanophotonic devices. *J. Nanophoton.* 8, 083096.
[40] Sun, F. L., Zhang, C. H., Li, D., You, F. T., Liang, C. J., Wang, Y. (2025). Tabulated values of the Shockley–Queisser limit for tandem solar cells. *Phys. Status Solidi A* 222, 2400524.
[41] Parathraju, P., Umasankar, P. (2025). Performance evaluation of ultrathin CdTe-based solar cells with dual absorbers via SCAPS-1D simulation. *Sci. Rep.* 15, 26428.
[42] Zapukhlyak, Z. R., Nykyruy, L. I., Wisz, G., Rubish, V. M., Prokopiv, V. V., Halushchak, M. O., Lishchynskyy, I. M., Katanova, L. O., Yavorskyi, R. S. (2020). SCAPS simulation of ZnO/CdS/CdTe/CuO heterostructure for photovoltaic application. *Phys. Chem. Solid State* 21, 660–668.
[43] Venkatesh, R., Singh, P. K., Bashir, M. N., Lee, J. S., Yaswanth, K. K., Soudagar, M. E. M., Hossain, I., Obaid, S. A., Alharbi, S. A. (2025). Performance study of cadmium telluride solar cell featured with silicon thin film made by sol-gel route. *Silicon* 17, 191–203.
[44] Candelas-Urrea, V. A., Villa-Angulo, C., Hernández-Fuentes, I. O., Morales-Carbajal, R., Villa-Angulo, R. (2024). All-layer electro deposition of a CdTe/$Hg_{0.1}Cd_{0.9}$Te/CdTe photodetector for short- and mid-wavelength infrared detection. *Coatings* 14, 1133.
[45] Khatri, I., Kasik, C., Sites, J. R. (2024). Performance of state-of-the-art CdTe-based solar cells: what has changed. *IEEE J. Photovoltaics* 14, 745–751.
[46] Mallick, R., Li, X., Reich, C., Shan, X., Zhang, W., Nagle, T., Bok, L., Bicakci, E., Rosenblatt, N., Modi, D., et al. (2023). Arsenic-doped CdSeTe solar cells achieve world record 22.3% efficiency. *IEEE J. Photovoltaics* 13, 510–515.
[47] Metzger, W. K., Miller, D. W., Mallick, R., Li, X. P., Zhang, W., Wang, I., Polizzotti, A., Ablekim, T., Cao, D. H., Hamilton, D. C.,

et al. (2022). As-doped CdSeTe solar cells achieving 22% efficiency with −0.23%/°C temperature coefficient. *IEEE J. Photovoltaics* 12, 1435–1438.

[48] Gloeckler, M., Sankin, I., Zhao, Z. (2013). CdTe solar cells at the threshold to 20% efficiency. *IEEE J. Photovoltaics* 3, 1389–1393.

[49] Shen, X. Q., Jiang, S. H., Wang, X. D., Zhou, H., Yu, Z. Q. (2023). Suppressing optical losses in solar cells via multifunctional and large-scale geometric arrays. *Nanomaterials* 13, 2766.

[50] Huang, P. G., Zhang, Q. L., Guan, Y. L., Xiao, Y., Wen, M. R., Hu, Y. J., Huang, L. (2025). Suppressing nonradiative recombination and enhancing hole density in $CdSe_xTe_{1-x}$ solar cells through as doping and se alloying: a hybrid functional study. *J. Phys. Chem. C* 129, 16392–16398.

[51] Wu, H. B., Lu, H., Li, Y. G., Zhou, X., Zhou, G. Q., Pan, H. L., Wu, H. Y., Feng, X. D., Liu, F., Vandewal, K., et al. (2024). Decreasing exciton dissociation rates for reduced voltage losses in organic solar cells. *Nat. Commun.* 15, 2693.

[52] Oni, A. M., Mohsin, A. S. M., Rahman, M. M., Hossain Bhuian, M. B. (2024). A comprehensive evaluation of solar cell technologies, associated loss mechanisms, and efficiency enhancement strategies for photovoltaic cells. *Energy Rep.* 11, 3345–3366.